Performance of Dispersed Fringe Sensor in the Presence of Segmented Mirror Aberrations – Modeling and Simulation

Fang Shi, Scott A. Basinger, and David C. Redding

Jet Propulsion Laboratory, California Institute of Technology, Pasadena, CA 91109

ABSTRACT

Dispersed Fringe Sensing (DFS) is an efficient and robust method for coarse phasing of a segmented primary mirror such as the James Webb Space Telescope (JWST). In this paper, modeling and simulations are used to study the effect of segmented mirror aberrations on the fringe image, DFS signals and DFS detection accuracy. The study has shown due to the pixilation spatial filter effect from DFS signal extraction the effect of wavefront error is reduced and DFS algorithm will be more robust against wavefront aberration by using multi-trace DFS approach. We also studied the JWST Dispersed Hartmann Sensor (DHS) performance in presence of wavefront aberrations caused by the gravity sag and we use the scaled gravity sag to explore the JWST DHS performance relationship with the level of the wavefront aberration. This also includes the effect from line-of-sight jitter.

Keywords: wavefront sensing and control, dispersed fringe sensor, segmented mirrors, wavefront aberration, JWST

1. INTRODUCTION

A coarse phasing technique using a dispersed fringe sensor (DFS) has been developed to phase the segmented primary mirror of the James Webb Space Telescope (JWST) during its initial deployment [1]. Over the years the DFS algorithm has been successfully demonstrated on various laboratory testbeds [2, 3, 7] as well as on the Keck Telescope [4, 5, 6]. Using simulations based on diffraction as well as realistic optical models we have carried out series studies intent to better understand the formation of DFS fringe and various factors that affect the DFS algorithm performance. In our paper published in the same conference two years ago [8], we studied the factors that determine the properties of a DFS fringe, such as segment geometric shape, pupil sparseness, grism dispersion orientation, image sampling, detector noise, etc… In the paper conclusion we pointed out one the major effect for the DFS performance is the segment mirror aberrations.

In this paper we continue our DFS performance study using simulation and optical modeling. We have concentrated in understanding the effect from wavefront aberrations on DFS. This includes the aberration effect on dispersed fringe image formation, DFS signal, and DFS piston detection accuracy. In this study we used both simulations based on diffraction from exit pupil and a realistic JWST ground integration and test (I&T) optical model. With the presence of wavefront aberrations we compared the performance between two different DFS algorithm approaches, namely single trace DFS and multi-trace DFS, and has shown that that multi-trace DFS approach performs much better when the system has large wavefront aberrations compared with the single trace DFS. We also use the JWST ground I&T model and the scaled gravity sag on the JWST segment deformation to evaluate the performance of JWST's Dispersed Hartman Sensor (DHS). Besides the conventional wavefront aberration we also studied effect of line-of-sight jitter on JWST DHS performance.

This work is organized as follows. In Section 2 we present results from our diffraction based simulation. We will exam the wavefront aberration effect on DFS image and signal. We then compare the performance of two DFS algorithm approaches. In Section 3 we describe the JWST ground I&T model and effect of gravity sag. We also added the line-of-sight (LOS) jitter in the DHS fringe to understand its effect on DHS performance. Finally we present our conclusions and outline our future work in Sections 4.

2. WAVEFRONT ABERRATION EFFECT ON DFS AND MULTI-TRACE DFS

The dispersed fringe sensor uses a transmissive grism as the dispersing element. The grism disperses the light from a broadband point source according to its wavelength, forming a spectrum on the camera. The wavelength dispersion relation along the dispersion direction x is

$$\lambda(x) = \lambda_0 + \frac{\partial \lambda}{\partial x} x = \lambda_0 + C_0 x \tag{1}$$

where λ_0 is the central wavelength and C_0 is the linear dispersion coefficient, which depends on the characteristics of the grism. An approximate but general derivation [4] has shown that the intensity along the fringe has the form of,

$$I(x, y) = I_0 \left[1 + \gamma \cos\left(\frac{2\pi}{\lambda(x)} \delta + \varphi(y) \right) \right] \tag{2}$$

where $I(x,y)$ is the dispersed fringe intensity along the dispersion coordinate x, I_0 is the mean intensity, γ is the fringe visibility which varies between 0 and 1, and φ is a phase constant that depends on where the DFS fringe is extracted, and φ is zero at the fringe center ($y = 0$). To explore the DFS fringe properties we rely on computer simulations, which numerically calculate the broadband point spread function (PSF) formed by the segment-DFS imaging system. By repeatedly adding PSFs incoherently over the wavelength range to form a dispersed broadband PSF, the numerical simulations provide an accurate and realistic rendering of a DFS fringe that allows us to study the DFS performance under various segment geometries and dispersion conditions.

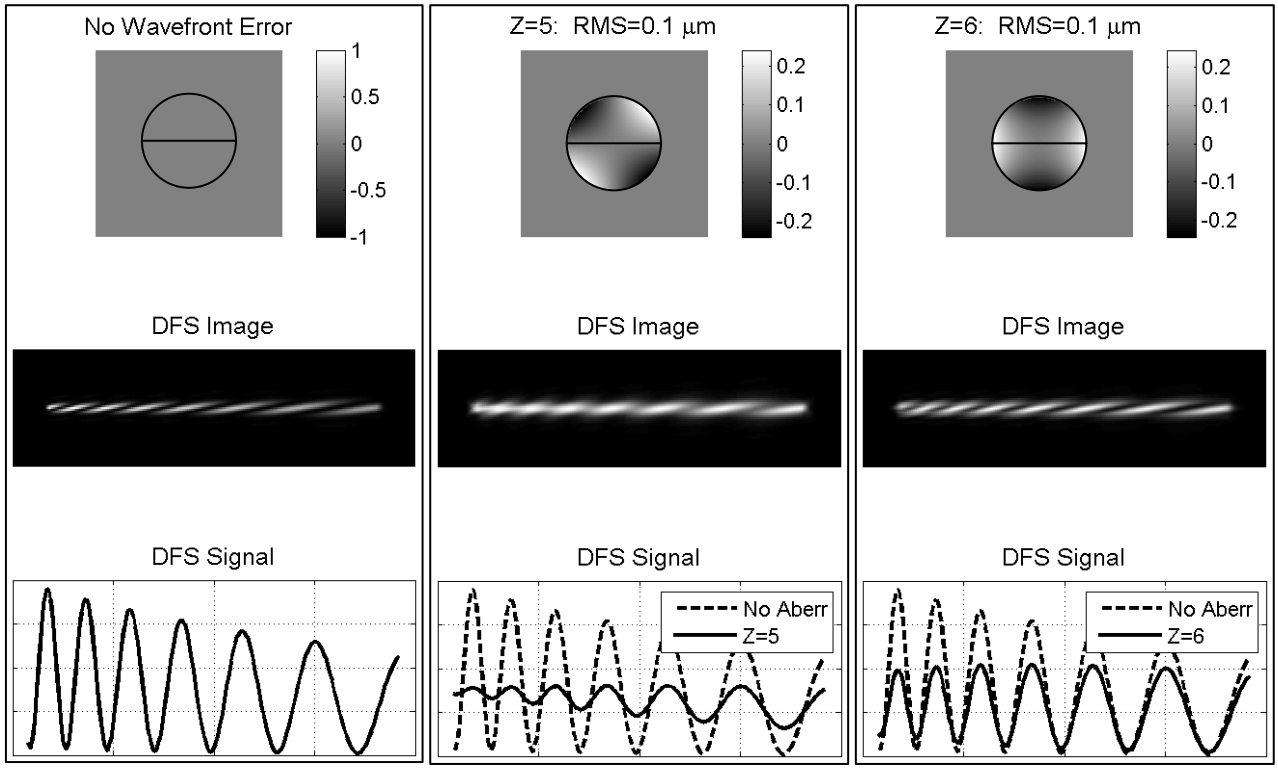

Figure 1. Simulated DFS fringe images and DFS signals with no wavefront aberration (*left*), with 0.1 μm (rms) 45° astigmatism (*middle*), and 0.1 μm (rms) 0° astigmatism (*right*). The two segments split the circular aperture. OPDs (*top*) do not include the segment piston to accentuate wavefront error. Wavelength increases from left to right.

To under stand the effect of wavefront aberrations on the DFS fringe images and DFS signals. We use the simulation based on diffraction. In the simulation we choose a circular aperture and two segments split the circular aperture. A circular aperture makes it easier to add aberration in Zernike terms. We simulated DFS fringes under each Zernike aberration terms. Fig. 1 shows the example of the effect of wavefront aberration on the dispersed fringe. When there is no wavefront aberration the DFS fringe formed shows a high sharp fringe pattern and DFS signal extracted presents high contrast modulation. When a RMS 0.1 μm 45° astigmatism (Zernike term Z = 5) is added to the wavefront and fringe image is significantly blurred. Compared with aberration free the DFS signal level is lower and modulation reduced. Also, as expected the wavefront aberrations affect more on the shorter wavelength end of spectrum than that of longer wavelength, further reducing the DFS signal modulation. However, when the wavefront has the same amount of aberration but in 0° astigmatism (Zernike term Z = 6) the loss of fringe contrast is not as significant as that of 45° astigmatism. This has clearly demonstrated that the type of the wavefront aberration is also important in determine the effect of wavefront aberrations. The simulation has shown that those wavefront aberration which forms larger PSF size along the dispersion directions causes more DFS degradation.

Because wavefront aberration causes system forms larger PSF the DFS signal extracted from a row of the pixels from the fringe will have lower intensity. Compared with aberration free system this will lead to lower signal-to-noise ratio (SNR). In another hand, because the DFS signal comes from one single row of pixels with pixel size usually being a fraction of PSF size. The pixels in DFS signals act as a spatial filter for their corresponding wavelength. In other words, each pixel samples only part of aberrated PSF, therefore suffers less impact from the wavefront aberrations. In Figure 2 we generated a random wavefront aberrations using the first 50 Zernike terms using a power law of -1 to damp the strength of high order aberration terms. The filtered OPD from a single pixel is much less than that of the original OPD.

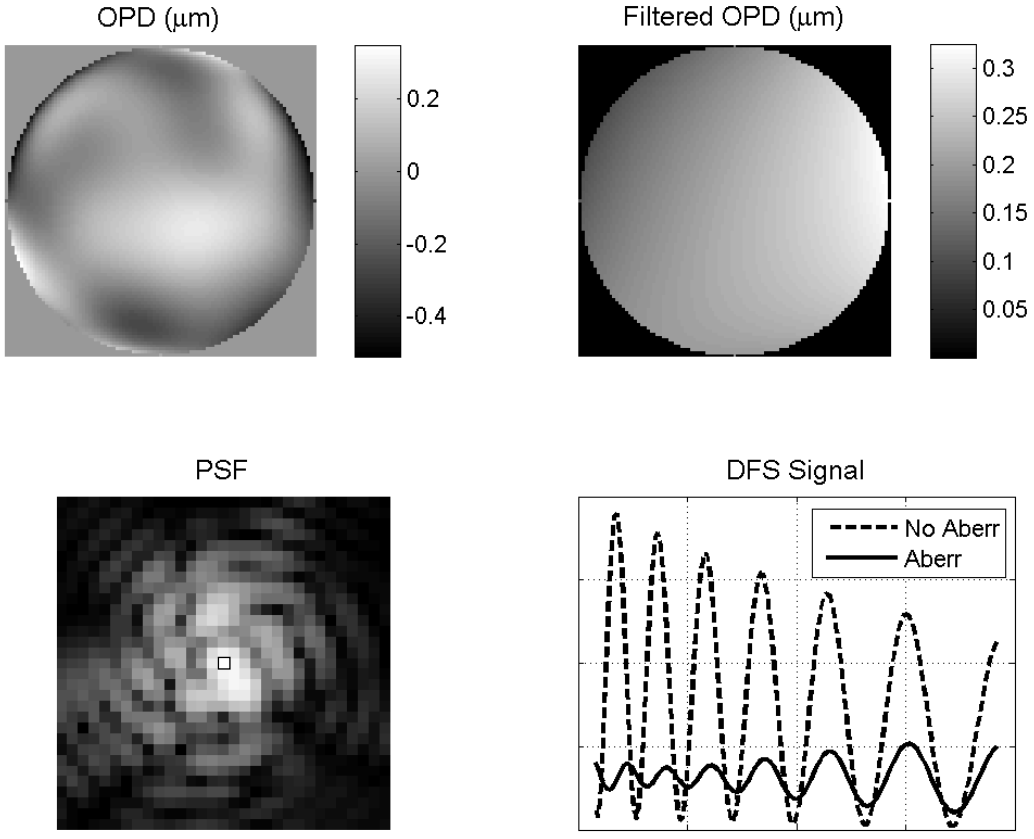

Figure 2. Illustration of spatial filter by pixilation. The original OPD (*upper left*) has aberration with rms value of 0.136 μm and *lower left* shows the corresponding PSF at center wavelength of the DFS. When spatially filtered by the single pixel indicated by a black box on the PSF image, the filtered OPD (*upper right*) rms value reduced to 0.011 μm. The plot in *Lower right* compares the raw DFS signal between that from this aberrated OPD to that of ideal OPD.

Because of this "spatial filter" effect from pixel the resulted DFS signal from the aberrated system, though has less mean intensity, can still have moderate visibility. This enables DFS to be able to tolerate moderate wavefront aberrations.

During our DFS algorithm development we have proposed the concept of "multi-trace DFS" to increase the piston detection accuracy [3]. This algorithm has since then been implemented as an optional DFS fringe analysis module and user can select either "single-trace DFS" or "multi-trace DFS", with the former option being mostly used for quick fringe analysis and piston detection. With a proper sampled image system the PSF several times the size of pixel. In multi-trace DFS, instead of extract one middle row of pixels from DFS fringe, multiple rows of the pixels are extracted along the dispersion direction as the DFS signals. Each row of DFS signal are then processed independently and piston detected are then averaged to provide the final piston detection from the fringe. A few criteria based selection and weighting are involved in the multi-trace DFS. Before the fringe analysis criteria based on fringe profile is used to select the rows of DFS signals with suitable SNR. After the fringe analysis we also apply weight on the results from each individual result depending on a suit of criteria for fitting goodness.

The multi-trace DFS is very useful in increasing the algorithm robustness against wavefront aberrations. Because of the "pixilation spatial filter effect" each row of DFS sees different part of high order wavefront aberration and by averaging the effect of wavefront aberration can be reduced, assuming the wavefront aberration is random in nature. Also, compared with the single-trace DFS, using multiple rows of pixel as the DFS signals we can regain some of the loss of signal-to-noise ratio due to the larger PSF size from wavefront aberrations.

To compare the DFS performance we use simulation model to carry a Mote Carlo study in which we generated 20 random wavefront consist of first 50 Zernike modes (not include first three terms, i.e. piston and tilts). A power law of -1 is applied to reduce the power of high order aberrations. We then scale amplitude of the same 20 cases of wavefront to provide wavefront with rms aberration from 0.06 μm to 1.20 μm which is equivalent to λ/125 to 1.6λ while the center wavelength DFS is at λ = 0.7 μm. DFS fringes are then generated for each of those wavefronts at together with a segment wavefront piston of 8 μm. We then use single-trace and multi-trace DFS to analyze these fringe. Figure 3 compares the performance between single-trace DFS and multi-trace DFS on aberrated DFS fringes in terms of piston detection error, which defines as the piston detected by the algorithm minus the piston applied (8 μm), and the piston detection rate. The Monte Carlo simulation has shown that multi-trace DFS has smaller detection error compared with the single-trace DFS. More importantly, as the wavefront aberration increases the single-trace DFS quickly becomes un-reliable shown as the successful detection rate decreases while the multi-trace DFS holds on very well.

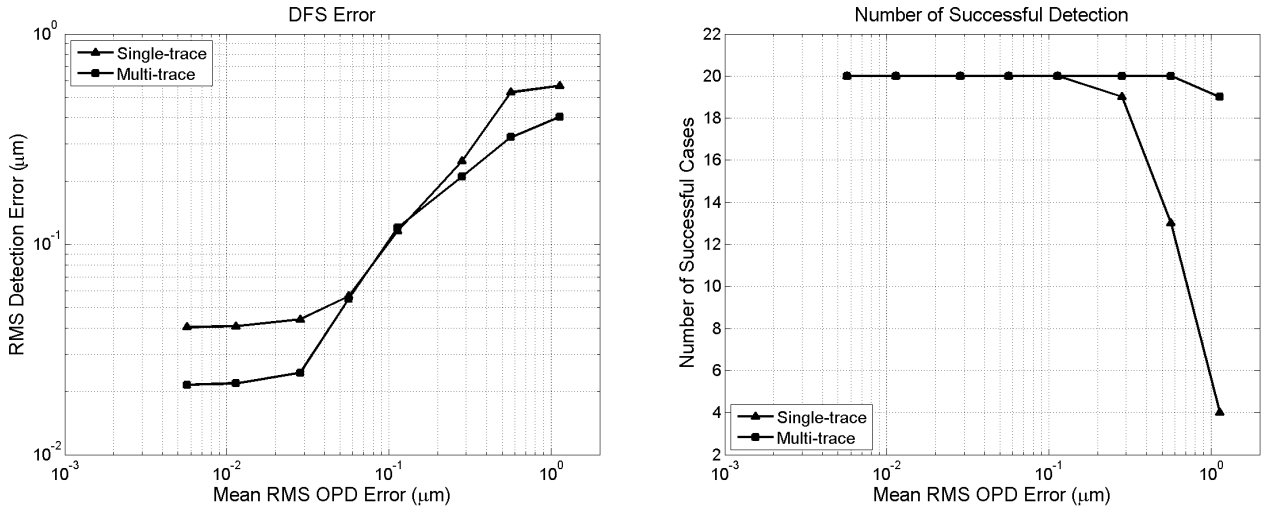

Figure 3. Compare the performance of single-trace DFS and multi-trace DFS against the wavefront error. The plot on the *left* shows the DFS piston detection error against wavefront error. The detection error on the plot is the rms of all successful detections from the 20 cases and the wavefront error value is the mean of the rms OPD from 20 cases. The plot on the *right* shows the number of case which has successful piston detection. There are total 20 cases at each wavefront aberration strength.

3. JWST DHS PERFORMANCE UNDER SEGMENT MIRROR GRAVITY SAG

3.1 JWST ground integration and test model

Modeling study has been carried out to investigate the JWST DHS performance under the wavefront aberration due the JWST segmented mirror gravity sag during the ground integration and test (I&T). JWST has 18 segments in hexagonal layout and it uses the Dispersed Hartmann Sensor (DHS) for segment mirror coarse phasing. DHS is a dispersed fringe sensor based device. Compared to a DFS grism DHS has, in addition to the grism, an array of cross-disperse displacement prisms which deviate the fringes from segment edges away from each other which enables simultaneously forming dispersed fringes from 10 segment edges in a single image. Two DHS devices in the JWST's NIRCam pupil wheel will measure 20 inter-segment edge heights. From the 20 inter-segment edge height measurements, one can reconstruct the 18 segment commands to coarse phase the segmented primary mirror.

Before launch JWST will go through series of integration and test in ground. One of the test will be coarse phasing with DHS. Due to the Earth's gravity JWST's segmented mirror will suffer mirror surface deformation, so called gravity sag. All JWST segments have the correcting capability of 6-degree freedom rigid body motion and center-of-curvature. Correction will be applied to compensate the gravity sag. However, even after these corrections the modeling has shown that there will be about rms 300 nm wavefront error left in the system. JWST mirror gravity sag during ground I&T is used as the wavefront aberration to study the DHS performance under wavefront Aberration

A realistic optical model is setup using MACOS, an optical modeling tool developed at JPL and has been successfully used for many flight project. This MACOS model includes JWST telescope and NIRCam with DHS, a JWST science instrument which also being used as the wavefront sensing and control for JWST. The model is set for JWST's ground I&T with an auto-collimate flat (ACF) in a double pass configuration. The original mirror deformation from gravity sag comes from a structural finite element model and we make a center of tilt and curvature correction to original gravity sag and applied to the residual mirror surface figure error directly to the mirror surface in the MACOS model. To simulate the various strengths of wavefront aberrations the gravity sag is scaled from by a factor varies from 0.25 to 3.0. To reduce the time required for the model calculations we have selected only 2 out of 10 fringes from each DHS for modeling and performance studying. The selected two fringes represent the two types of DHS subapertures and results should apply to other DHS fringes without loss of the generality. The two subapertures selected in 0° DHS (see Figure 5) are the lower-middle one and lower-right one. For the 60° DHS the selection is similar to that of 0° DHS but rotated counter-clockwise by 60°. So the selected two are the middle one near lower-right portion of OPD map and another one is one most toward upper-right. The selected two subaperture in each DHS device represent the two types of the subapertures with the one in the middle has equal area across the segment edge (Type 1) while the subaperture at edge has an unequal area between the two segments (Type 2).

3.2 Effect of wavefront aberration on JWST DHS performance

Figure 4 shows the modeled result of full aperture JWST wavefront (OPD) with and without gravity sag and corresponding PSF. The OPD is after the double pass and measured in the NIRCam exist pupil. For the full JWST aperture without gravity sag the rms wavefront is 0.058 μm with peak-to-valley of 0.272 μm. When including the gravity sag the rms and peak-to-valley wavefront becomes 0.315 μm and 1.741 μm. The PSF under the gravity sag has clearly been depredated. However, when see through the DHS devices each DHS subaperture only sees a portion of the full wavefront, as shown in Figure 5. Among the DHS subapertures the rms wavefront is reduced and Figure 6 shows the values for these subapertures we selected in out modeling.

To understand the JWST DHS performance under the wavefront aberration we use the gravity shown in Figure 6 and apply a scale factor which varies from 0.25 to 3.0. The process starts with using the MACOS model to generate DHS fringe images for the selected subapertures. Figure 7 shows the example of DHS fringes with and without gravity sag. Also shown in Figure 7 are the effect of system line-of-sight jitter which is discussed later. In our Monte Carlo test, for each gravity sag scale factor we generate 20 case of random piston map on the JWST segments and for each piston map model generate a broadband NIRCam image contains DHS fringe from selected subaperture. The wavelength we used is centered at 1.36 μm and spectral range for our modeling is from 1.16 – 1.56 μm. Then multi-trace DFS algorithm is used to extract and analyze each fringe and the detected edges height is then compared with the edge height from the piston map applied. For each subaperture at the each wavefront aberration scale the rms piston detecting errors from the

Figure 4. JWST wavefront with (*left*) an without (*right*) gravity sag. The OPD (*upper panel*) is in unit of micron of wavefront and is plot in the same linear scale for comparison. The PSF (*lower panel*) is logarithmically stretched.

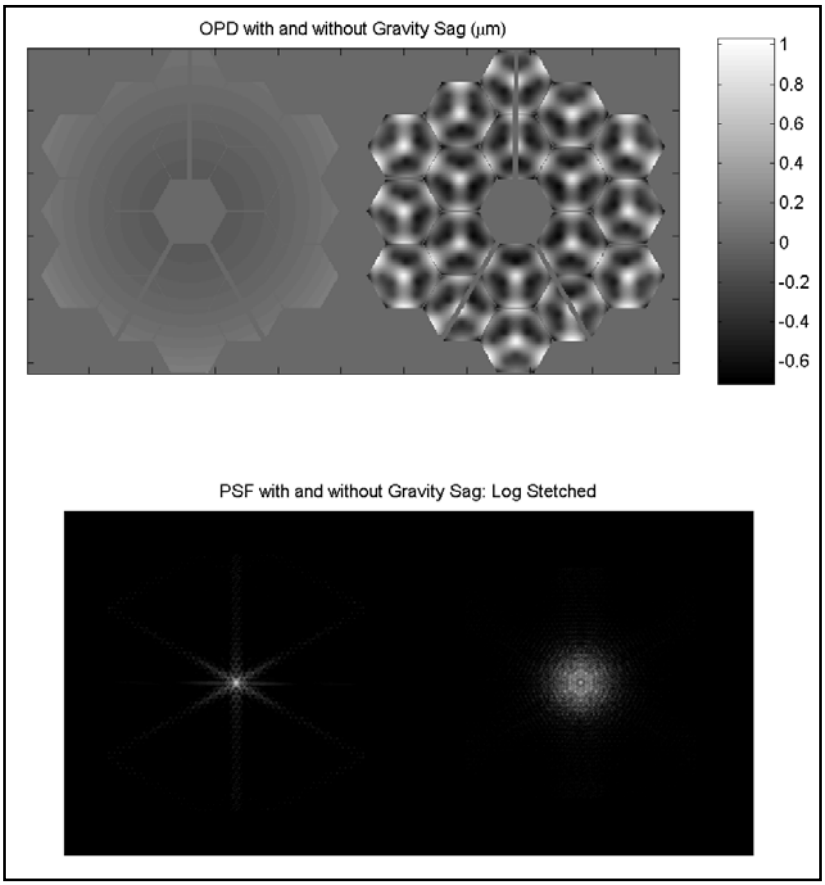

Figure 5. JWST wavefront through 0° (*left*) and 60° (*right*) DHS devices. The *upper panel* is when there is no gravity sag and *lower panel* is that with gravity sag. Again, wavefront is in unit of micron.

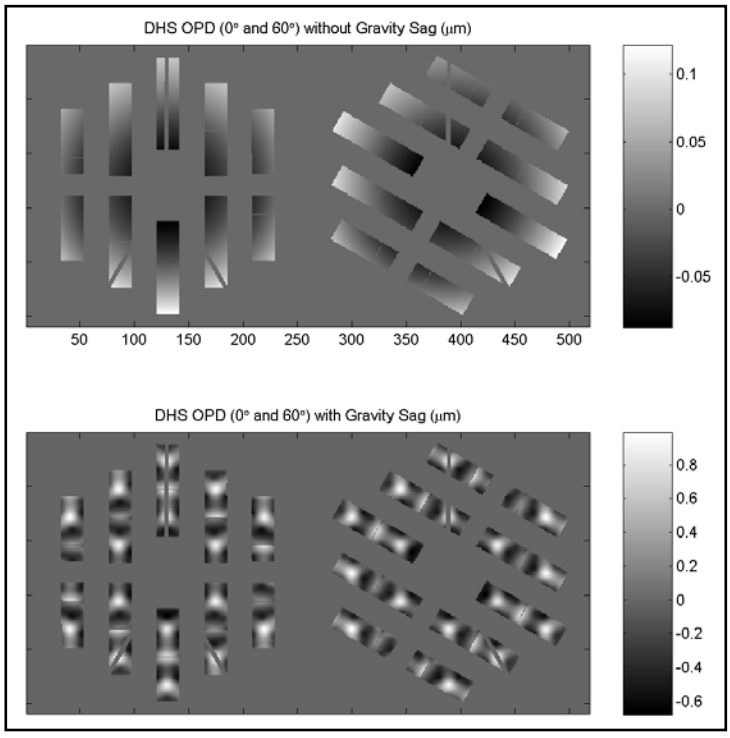

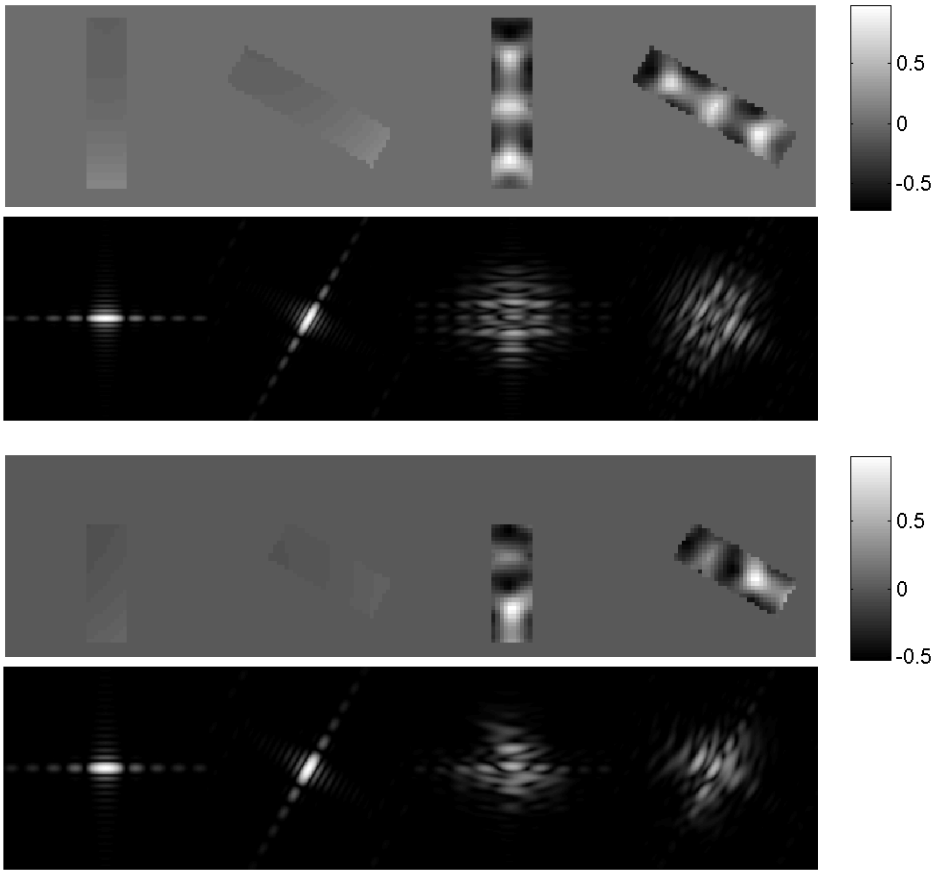

Figure 6. The wavefront for the selected DHS subapertures and their corresponding PSFs with and without gravity sag. The top row is the OPDs for the Type 1 subapertures. The two on the left are 0° and 60° DHS without gravity sag and their rms wavefront errors are 0.078 and 0.073 μm. The two on the right are that with gravity sag and their rms wavefront errors are 0.372 and 0.358 μm. The second row is the corresponding PSFs at center wavelength from the Type 1 subapertures. The third row is the Type 2 DHS subapertures 0° and 60° with and without the gravity sag. The rms wavefront errors are (from left to right): 0.032, 0.025, 0.317 and 0.307 μm. The last row shows the PSFs formed by the Type 2 subapertures. OPDs within each panel are plotted in the same linear scale for comparison and the PSFs are all logarithmically stretched to accentuate the details in the diffraction.

20 cases are calculated to evaluate the JWST DHS performance under this aberration for this subaperture. We also calculate the DHS fringe mean and peak-to-valley visibility for each gravity scale. The results are plotted in Figure 8 and 9

From the DHS fringes in Figure 7 we can see that DHS fringe formed with gravity sag has broken into a multiple braids fringe. Because the wavefront error affects the PSF differently at different wavelength the resulted fringe has complicated structure. Instead of two peaks for the no gravity case there are multiple peaks across the dispersion. This is because the wavefront seen by the DHS subaperture has the clumps which cause the PSF break up across the dispersion direction. Our study has shown that without the multi-trace DFS process the algorithm fails to detect the wavefront piston. in many cases

Figure 8 and 9 shows the results from the modeling study on the JWST DHS performance under the wavefront aberration. From Figure 8 we can see that as the wavefront aberration increases the DHS detection error increases for all the DHS subapertures. However, upon close examination we can see there are differences between the different

subapertures even at the similar rms wavefront aberration. There many sources that may cause the difference. One of them is that there are different types of the wavefront errors among the subapertures. As illustrated in Section 2 the wavefront aberration effect on DFS is highly depend on the type or the nature of the aberrations. Looking closely we can see that there are difference in the content of gravity sag among the DHS subaperture we modeled. Also slightly difference is that the OPD sampling are slightly different between 0° and 60° DHS. This partly because the binning effect for the smaller MACOS size we chose (going into larger MACOS size will significantly increase the computation time). Because OPDs for 60° DHS are sampled with fewer points they appear to be containing less high order aberration. This may partly explain why 60° DHS seems have better performance than that of 0° DHS. Plots in Figure 9 show the DHS fringe visibility drop as the wavefront error increase. The Type 2 subapertures have lower visibility to start off with because the aperture contains unequal areas from the two segments. The curves show that the fringe visibility dropping quickly to around 0.3 – 0.4 at rms OPD of 0.5 μm. Then the visibility curve leveled off. Coincidently, the DHS detection errors begin to increase quickly after rms OPD errors reach 0.5 μm. We have notice that this where the wavefront error smear out most of the blue end of spectrum in the DHS fringes causing larger detection error. One mitigate to this is to shift the piston detection toward red end of spectrum because, as mentioned in Section 2, the wavefront aberration affect more on the light in shorter wavelength region.

3.3 Effect of line-of-sight jitter on the JWST DHS performance

In our modeling study of JWST DHS performance we also studied the effect of line-of-sight jitter (LOS) on JWST DHS's performance. LOS is a special kind of wavefront aberration. The effect represents an accumulation of many random global wavefront tilts. If we assume the LOS jitter is random in nature then we can use a Gaussian blurring kernel to represent the LOS jitter and the full-width-half-max (FWHM) width can be used to quantify the strength of LOS jitter. We use the Gaussian jitter kernel convolving with the DHs fringe images to simulate the DHS fringe with LOS jitter. The jitter width is in unit of pixel. For NIRCam the pixel scale is about 30 milli-arcsecond per pixel. Figure 7 shows an example of LOS jitter on the fringe image. We have chosen two wavefront aberration cases to study the LOS jitter effect. One is the fringe without gravity sag and another is that with the 1X gravity sag. We then apply jitter kernel with different FWHM widths to simulate the different levels of jitter strength. Multi-trace DFS algorithm is used to detect the pistons and rms piston value from the 20 cases at each jitter level is calculated. Also calculated is the fringe visibility. Figure 10 shows the rms DHS detection errors against the FWHM jitter and Figure 11 shows the fringe visibility against the jitter. Plots in Figure 11 have shown that as the LOS jitter increases the fringe visibility drops quickly with aberrated (1X gravity sag) fringes have lower visibility to start off with. However, there seems lack of any correlation between the LOS jitter level and the DHS detection error. The curves, especially that from the case without gravity sag, remain flat as the jitter level increase from no jitter to 8 pixels (FWHM) jitter and mean fringe visibility drops to around 0.1. This indicates that the DFS algorithm is surprisingly robust against the line-of-sight jitter.

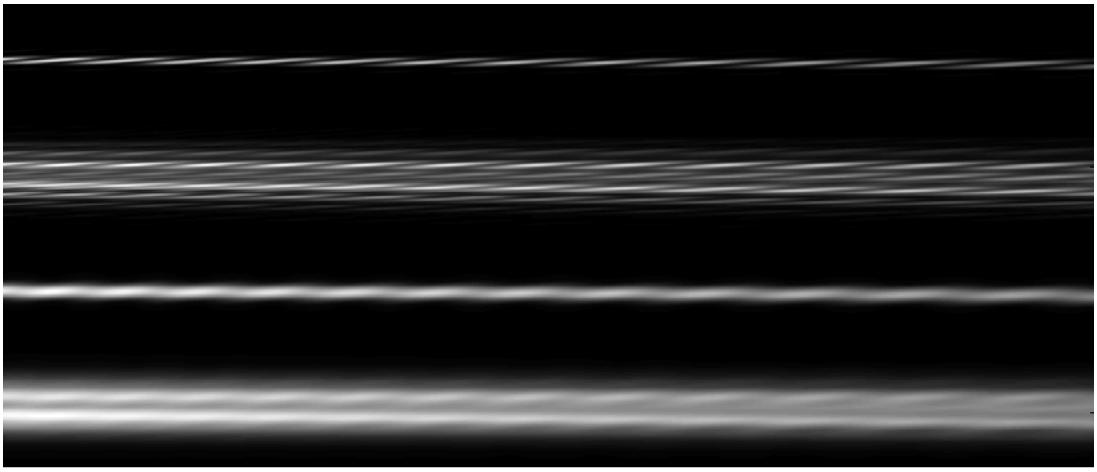

Figure 7. Sample DHS fringe images. All image come from the same segment edge height and from the subaperture Type 1 in the 0° DHS. Fringe images from top to bottom: no gravity sag and no line-of-sight (LOS) jitter; with 1X gravity sag and no LOS jitter; no gravity sag and with LOS jitter of about 6 pixels full-width-half-max (FWHM); with 1X gravity sag and with 6 pixel (FWHM) LOS jitter.

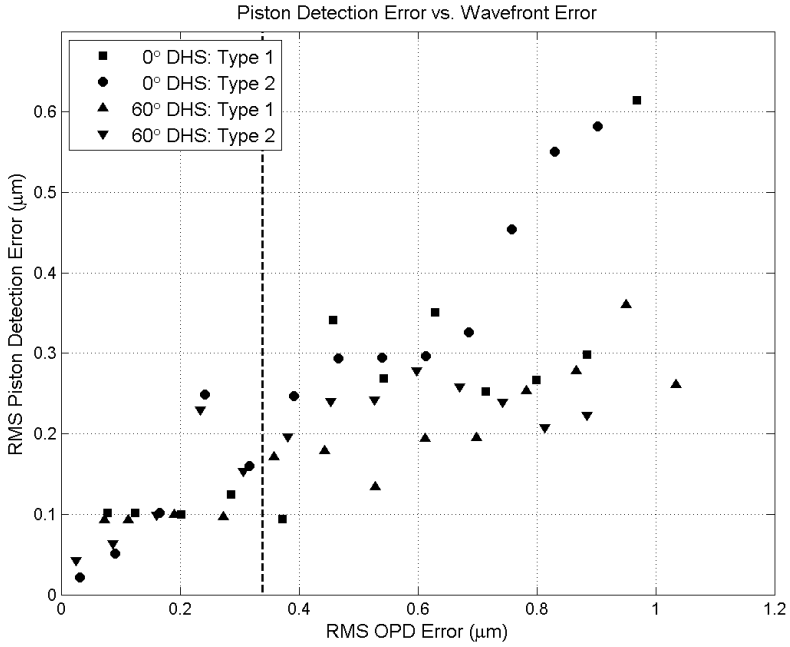

Figure 8. JWST DHS piston detection error against wavefront error simulated by scaling the gravity sag. The DHS device and DHS subaperture type are denoted in the legend. The piston detection errors are rms detection errors for the 20 cases of random piston map applied at each wavefront error scales. The 1X gravity sag (scale factor 1.0) are indicated by the dashed line.

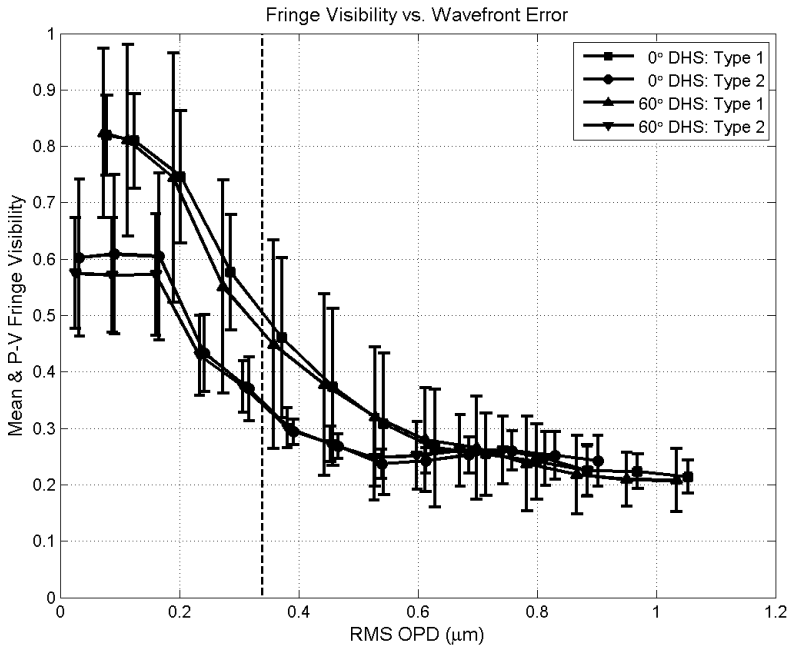

Figure 9. JWST DHS fringe visibility against wavefront error simulated by scaling the gravity sag. The DHS device and DHS subaperture type are denoted in the legend. The curve shows both the mean visibility for the 20 random cases as well as the peak-to-valley visibility range in the 20 cases. The peak-to-valley values are plotted as the error bars in that the length of error bars equal to the peak-to-valley values. The 1X gravity sag (scale factor 1.0) are indicated by the dashed line.

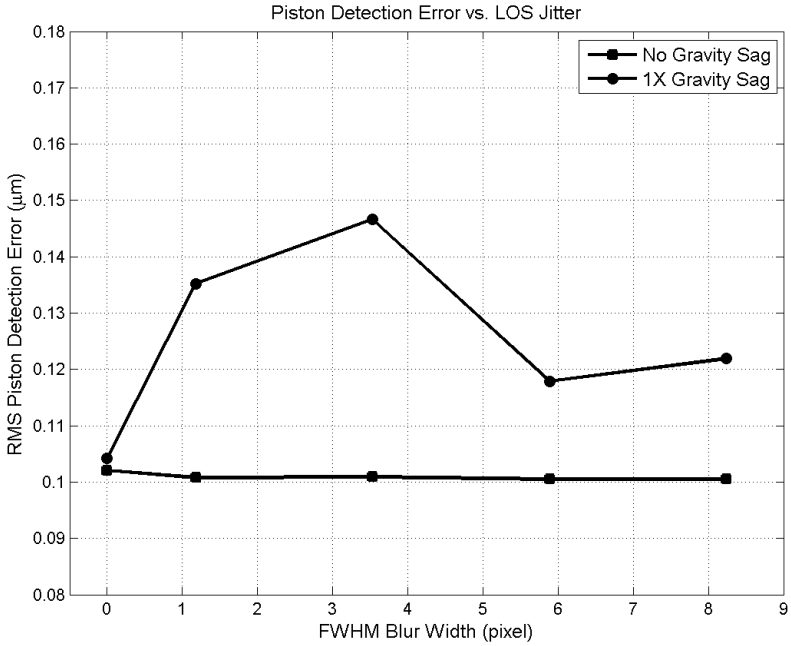

Figure 10. JWST DHS detection error against the line-of-sight jitter. The piston detection errors are rms detection errors for the 20 cases of random piston maps applied at jitter level. The jitter is represented with FWHM Gaussian kernel width in unit of pixel. Two aberration cases are plotted here: no gravity sag and 1X gravity sag from the subaperture of 0° DHS Type 1.

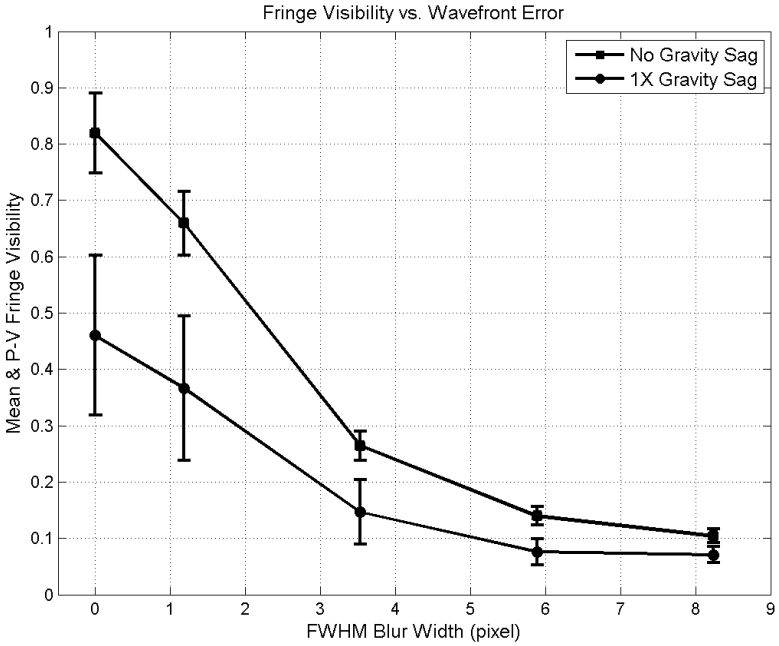

Figure 11. JWST DHS fringe visibility against wavefront error simulated by scaling the gravity sag. The curve shows both the mean visibility for the 20 random cases as well as the peak-to-valley visibility range in the 20 cases. The peak-to-valley values are plotted as the error bars in that the length of error bars equal to the peak-to-valley values. The jitter is represented with FWHM Gaussian kernel width in unit of pixel.

4. SUMMARY

Diffraction based broadband PSF generator and MACOS modeling tools are used to study the effect of wavefront aberration on the performance of DFS. This paper has presented results from two cases: (1) with general DFS under wavefront error from a randomly generated aberration consists of first 50 Zernike modes in a power law of -1; (2) JWST DHS under the scaled ground I&T gravity sag, which consists of a unique wavefront properties. Line-of-sight jitter has also applied to this case. From the simulation result we conclude:

- Wavefront aberrations will lower the DFS fringe visibility and DFS signal signal-to-noise ratio.
- The specific effect of wavefront aberration on DFS depends on the aberration type and the aberration which causes PSF elongation along the dispersion direction has the worst effect on DFS image contrast.
- Due to the “pixel spatial filter” effect the extracted DFS signal can tolerate moderate amount of wavefront aberrations.
- By averaging piston detection results from multiple traces extracted from fringe images, DFS can further increase its robustness against wavefront aberration. This is especially important when process the data from the wavefront aberration like the JWST ground I&T gravity sag.
- Modeling results have shown that gravity sag on the JWST segment mirror during ground I&T will lower the DHS fringe visibility by factor of 2–3X and lower the DHS signal intensity by factor of ~5X. At 1X gravity sag the rms DHS detection error is about 100 nm
- Line-of-sight jitter causes significant loss of JWST DHS fringe visibility and it affects more on the aberrated system. However, within the current simulation range there seems lack a strong correlation between the detection error and level of LOS jitter.

ACKNOWLEDGEMENTS

This research was carried out at the Jet Propulsion Laboratory, California Institute of Technology, under a contract with the National Aeronautics and Space Administration (NASA).

REFERENCES

[1] “Wavefront control for a segmented deployable space telescope,” D. Redding et al., *SPIE,* vol. **4013**, 546, Munich, Germany, Mar. 29-31, 2000.

[2] F. Shi, D. C. Redding, C. W. Bowers, A. E. Lowman, S. A. Basinger, T. A. Norton, P. Petrone III, P. S. Davila, M. E. Wilson, and R. A. Boucarut, "DCATT dispersed fringe sensor: modeling and experimenting with the transmissive phase plates," in *UV, Optical, and IR Space Telescopes and Instruments*, J. B. Breckinridge and P. Jakobsen, eds., Proc. SPIE **4013**, 757 - 762 (2000).

[3] F. Shi, D. C. Redding, A. E. Lowman, C. W. Bowers, L. A. Burns, P. Petrone III, C. M. Ohara, and S. A. Basinger, "Segmented mirror coarse phasing with a dispersed fringe sensor: experiments on NGST's Wavefront Control Testbed," in *IR Space Telescopes and Instruments*, J. C. Mather, ed., Proc. SPIE **4850**, 318 - 328 (2002).

[4] F. Shi, G. A. Chanan, C. Ohara, M. Troy, and D. C. Redding, "Experimental verification of Dispersed Fringe Sensing as a Segment Phasing Technique Using the Keck Telescope," *Appl. Opt.* **43**, No 23 (2004).

[5] F. Shi, G. A. Chanan, C. Ohara, M. Troy, and D. C. Redding, "Experimental verification of Dispersed Fringe Sensing as a Segment Phasing Technique Using the Keck Telescope," paper **5489-71**, SPIE Glasgow, UK (2004).

[6] M. J. Albanese, A. Wirth, A. J. Jankevics, T. Gonsiorowski, C. M. Ohara, F. Shi, M. Troy, G. A. Chanan, and D. S. Acton, "Verification of the James Webb Space Telescope coarse phase sensor using Keck Telescope," paper **6265-33**, *Space Telescopes and Instrumentation I: Optical, Infrared, and Millimeter*, SPIE Orlando, (2006).

[7] D. S. Acton, A. R. Contos, P. D. Atcheson, D. C. Redding, F. Shi, D. M. Shields, and T. C. Towell, "Demonstration of the James Webb Space Telescope commissioning on the JWST testbed telescope," paper **6265-25**, *Space Telescopes and Instrumentation I: Optical, Infrared, and Millimeter*, SPIE Orlando, (2006).

[8] F. Shi, D. C. Redding, J. J. Green, and C. M. Ohara, "Performance of the Segmented Mirror Coarse Phasing with a Dispersed Fringe Sensor: Modeling and Simulation," SPIE vol. 5487, 897 - 908, *Optical, Infrared, and Millimeter Space Telescopes*, John C. Mather Chair/Editor, 21-25 June 2004, Glasgow, Scotland, UK